



China Geology

Journal homepage: <http://chinageology.cgs.cn>
<https://www.sciencedirect.com/journal/china-geology>



A three-dimensional Moho depth model beneath the Yemeni highlands and rifted volcanic margins of the Red Sea and Gulf of Aden, Southwest Arabia

Amin Noman Al Kadasi*

Department of Geology, Faculty of Applied Science, Taiz University, Taiz 04, Yemen

ARTICLE INFO

Article history:

Received 17 June 2022
 Received in revised form 9 September 2022
 Accepted 9 October 2022
 Available online 23 May 2023

Keywords:

Bouguer gravity anomaly
 Earth gravitational model (EGM2008)
 Moho discontinuity
 Mantle upwelling
 Lithosphere-asthenosphere interaction
 Volcanic passive margin
 Isostasy
 Gulf of Aden
 Red Sea
 Arabian Peninsula

ABSTRACT

Knowing Moho discontinuity undulation is fundamental to understanding mechanisms of lithosphere-asthenosphere interaction, extensional tectonism and crustal deformation in volcanic passive margins such as the study area, which is located in the southwestern corner of the Arabian Peninsula bounded by the Red Sea and the Gulf of Aden. In this work, a 3D Moho depth model of the study area is constructed for the first time by inverting gravity data from the Earth Gravitational Model (EGM2008) using the Parker-Oldenburg algorithm. This model indicates the shallow zone is situated at depths of 20 km to 24 km beneath coastal plains, whereas the deep zone is located below the plateau at depths of 30 km to 35 km and its deepest part coincides mainly with the Dhamar-Rada'a Quaternary volcanic field. The results also indicate two channels of hot magmatic materials joining both the Sana'a-Amran Quaternary volcanic field and the Late Miocene Jabal An Nar volcanic area with the Dhamar-Rada'a volcanic field. This conclusion is supported by the widespread geothermal activity (of mantle origin) distributed along these channels, isotopic data, and the upper mantle low velocity zones indicated by earlier studies.

©2023 China Geology Editorial Office.

1. Introduction

The study area is located in the southwestern part of the Arabian Peninsula, enclosed between 12.5° N to 16.2° N and 43° E to 45° E. It extends northward along the western part of Yemen from the Red Sea and the Gulf of Aden ridges to khamir. The coastal plain of the Red Sea (the Tihama Plain) is up to 40–75 km wide extends parallel to the Red Sea and gently rises in elevation from sea level to about 200 m above sea level “ASL” at the foot of the Great Escarpment (Huchon P et al., 1991; Davison I et al., 1998). The Great Escarpment extends more than 1000 km from Yemen to the east of Makkah in Saudi Arabia and is marked by a sudden increase in altitude from 200 m to 1000 m ASL. On this escarpment (transitional zone between coastal areas and the plateau), the Yemeni highlands form a broad plateau along the eastern margin of the Red Sea with an average altitude of 2200 m ASL and a maximum altitude of 3660 m ASL at Jabal An Nabi Shuayb (J. N. Shuayb), southwest of Sana'a (Davison I

et al., 1998). The topography of the area, which is dominated by a thick sequence of Cenozoic volcanic rocks, is attributed to the interaction between mantle dynamics, lithosphere kinematics, magmatism, and surface processes (Davison I et al., 1998). Imaging Moho discontinuity is a key parameter to understanding the lithosphere-asthenosphere interaction, mechanisms of extensional tectonism and crustal deformation in volcanic passive margins (Sembroni A et al., 2016).

Seismic refraction experiments (Egloff F et al., 1991) show Moho depth varies from less than 13 km to 35 km below the Red Sea coast and the plateau, respectively. Receiver function analysis indicates variation in crustal thickness from 35 km below the plateau to 20 km and 22 km below the Red Sea and the Gulf of Aden coastal plains, respectively, (Ahmed A et al., 2013). A gravity survey along a profile extended between Ethiopian and Yemeni highlands revealed Moho depths ranging between 35 km below Sana'a and 22 km below the Tihama plain (Makris J et al., 1991). These studies sampled Moho depth beneath isolated regions, but it is still indistinct under the largest part of the study area. On the other side, global and continental/sub-continental three-dimensional crustal thickness models (e.g. Bassin CG et al., 2000; Chang SJ and Lee SV, 2011; Laske G et al., 2013; Mechie J et al., 2013; Stolk W et al., 2013; Gvirtzman Z et al.,

* Corresponding author: E-mail address: alkadasi2000@yahoo.com (Amin Noman Al Kadasi).

2016) generally image major changes in Moho topography but don't clearly reflect small scale variations, especially in geologically complex regions, such as the study area. However, the main objective of this work is to construct a continuous, three-dimensional model of Moho discontinuity undulation beneath the study area by inverting gravity data from the EGM2008. This model can be helpful in better understanding the kinematics of the lithosphere, mechanisms of crustal deformation and magmatic activity in the study area.

2. Geologic and tectonic setting

The southwestern part of the Arabian shield comprises gneisses and schists terrains intruded by granites of Pan-African age, 500 Ma to 800 Ma, (McCombe DA et al., 1994; Stewart SA, 2016). The Late Pan-African tectonic event (Najd fault system), dominated by large shear zones and NW-trending strike-slip faults (Levin G and Park J, 2000; Nehlig P et al., 2002; Stewart SA, 2016; Stern RJ and Johnson PR, 2019), heavily affected the shield and controlled the next geological architecture and tectonic regime in this region (Nehlig P et al., 2002; Al Kadasi AN, 2021). The crystalline basements exposed in the eastern, southern, and western parts of the area (Fig. 1).

The sedimentary rocks unconformably overlaying the basement and are dominated by Permian sandstones (*Wajid Formation*) in the northern part, Jurassic limestones (*Amran Group*) exposed mainly in the northern part, in addition to small exposures along the eastern and western boundaries of the plateau. The Cretaceous sandstones (*Tawilah Group*) are occurred in the form of isolated elongated exposures at the eastern and northern boundaries of the Cenozoic volcanics and along the uplifted rift shoulders formed by the Cenozoic extensional tectonism. The Quaternary deposits are mainly accumulated along the coastal plains of the Red Sea (Tihama basin) and the Gulf of Aden (Aden-Lahj basin).

A huge amount of magmatic materials erupted in three distinct phases during the Cenozoic in Yemen (Manetti P et al., 1991), concentrated in the western part, in response to the impingement of the Afar plume below the Afro-Arabia lithosphere and the subsequent processes that are eventually leading to the opening of the Red Sea and the Gulf of Aden (Capaldi G et al., 1987; Chiesa S et al., 1983, 1989; Chazot G et al., 1998; Ali MY and Watts AB, 2013; Stern RJ and Johnson PR, 2019; Sanfilippo A et al., 2021). A thick pile (about 2.5 km) of flood basalt and bimodal (basalt-rhyolite/ignimbrite) volcanic rocks erupted along N-S trending fissures throughout the whole plateau during the first phase (pre-rift, 30.9 Ma to 26.5 Ma) of magmatic activity (Civetta L et al., 1978; Chiesa S et al., 1989; Baker J et al., 1996; Chazot G et al., 1998). The second phase (syn-rift) is associated with the separation of Arabia from Africa (27.5 Ma to 16.1 Ma, Davison I et al., 1998; Stern RJ and Johnson PR, 2019). It is characterized by synchronous uplift, erosion, widespread crustal extension and intrusive magmatism (Menzies MA et

al., 1992, 1997; Davison I et al., 1994; Zumbo V et al., 1995; Baker J et al., 1996; Stern RJ and Johnson PR, 2019). The intrusive rocks (mostly alkali-granites, syenite, and less frequently diorite and gabbro) are concentrated mainly in the transitional zone between the plateau and the coastal plain in the form of dike swarms, plugs, domes, etc (Huchon P et al., 1991; Davison I et al., 1994). A higher amount of magma driven by shallow mantle processes in the asthenosphere (Baker J et al., 1996; Furman T et al., 2016; Stern RJ and Johnson PR, 2019; Sanfilippo A et al., 2021) is added to the lithosphere during the syn-rift period, at least 3 to 10 times the volume of erupted rhyolitic volcanic rocks and intrusive bodies (Davison I et al., 1998). The main part of the Yemen Trap Series (YTS) is formed during the first and second phases of magmatic activity. The third phase of magmatic activity (Post-rift < 6 Ma) is restricted along the margin of the Red Sea (Jabal An Nar volcanic area, near Al Mokha), Gulf of Aden (Aden volcanic line, extends from Aden to Perim Island), and on the Yemeni highlands (Sana'a-Amran, Dhamar-Rada'a and Marib-Sirwah fields) where the latest eruption occurred in 1937 in Dhamar-Rada'a field, (Manetti P et al., 1991; Chazot G et al., 1998). This phase was also driven by shallow mantle processes in the asthenosphere (Chazot G et al., 1998) and characterized by strato-type volcanoes, cones, domes, sheets, and lava flows.

Many earthquakes were recorded in the study area in historical times, including those occurred in Dhamar ($M_s=5.7$) in 1982 and in Al Uddyn, around Al Qafr ($M_s=4.4$) in 1991 (Ambraseys NN and Melville CP, 1983; Ambraseys NN et al., 1994; Alsinawi SA and Al Aydrus AA, 1999; Lemenkova P, 2021). Also, several geothermal manifestations (fumaroles, boiling pools, hot springs, and hydrothermal alteration) are distributed throughout the area (Minissale A et al., 2007). Both seismic and magmatic activities indicate an unstable dynamic situation in the area.

3. Data and methods

3.1. Gravity data

Simple Bouguer gravity anomaly data, 5' × 5' grid, of the study area were obtained from the EGM2008, developed by the US National Geospatial-Intelligence Agency (available at <http://icgem.gfz-potsdam.de/calcgrid>). This Model is a high-resolution global gravity model combines satellite, airborne and terrestrial gravity data (Pavlis et al., 2008). It overcomes the absence/scarcity of gravity data and provide the opportunity for a large scale regional and sub-regional studies of the earth geodynamics, isostasy, and kinematic of the lithosphere (e.g., Arabelos DN and Tscherning CC, 2010; Steffen R et al., 2011; Tenzer R et al., 2012; Evariste NH et al., 2014; Pal SK et al., 2015; Meliani O et al., 2016; Guy A et al., 2017). To produce the complete Bouguer gravity anomaly of the area (Fig. 2a), the effect of nearby topography is removed from the data by using the 5' × 5' grid global relief model ETOPO1 (Fig. 3; Amante C and Eakins BW, 2009)

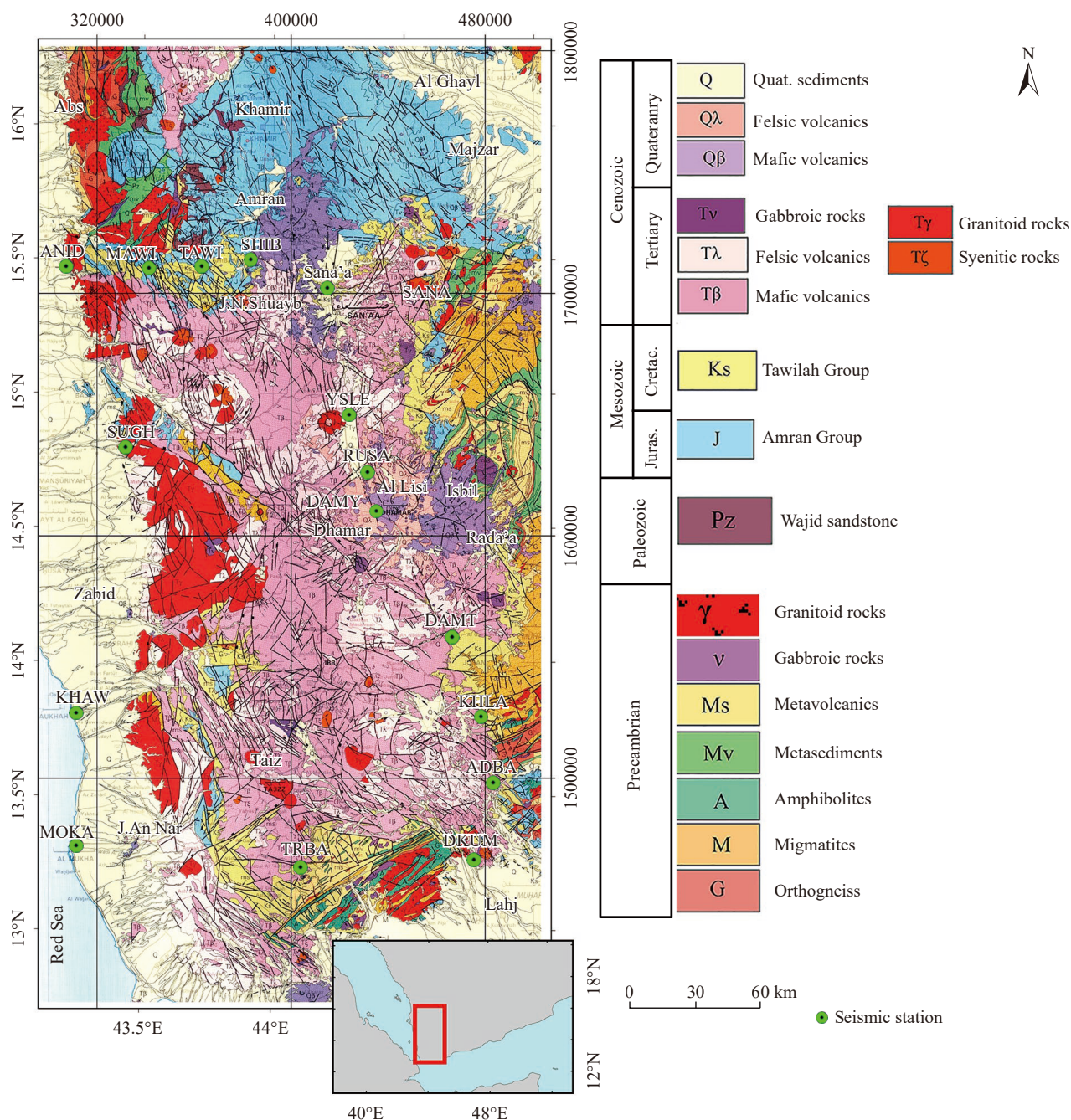


Fig. 1. Shows the main geologic features of the study area and its location between the ridges of the Red Sea and the Gulf of Aden (modified from Robertson PLC, 1990).

and an average topographic density (ρ_c) of 2670 kg/m^3 . A constant density is used for the sedimentary cover and the underlain igneous/metamorphic rocks to remove the effect of the Bouguer plate. Thus, the effect of the sedimentary cover (whose density is lower than that of hard rocks and induces negative Bouguer gravity anomalies) on the complete Bouguer gravity anomaly needs to be corrected. The sedimentary cover in the study area is mainly exposed in the Red Sea and Gulf of Aden coastal plains and in the northern part of the area, the Sana'a Basin (Fig. 1) and its thickness varies between 1 km and 4 km (Davison I et al., 1994, 1998; Egloff F et al., 1991; Ahmed A et al., 2013). Due to the absence of information related to the lateral variation in the

sedimentary cover thickness, the gravity anomaly of these rocks is calculated using an average thickness of 2.0 km and a density of 2.43 g/cm^3 and subtracted from the complete Bouguer gravity anomaly (Fig. 2a) in order to obtain the sediment corrected complete Bouguer anomaly (SCCBA) of the study area shown in Fig. 2b.

3.2. Inversion of gravity data

The gravity anomaly caused by topographic variations “h (x, y)” on a constant density contrast two-dimensional surface is calculated by equation (1) according to Parker RL (1972)

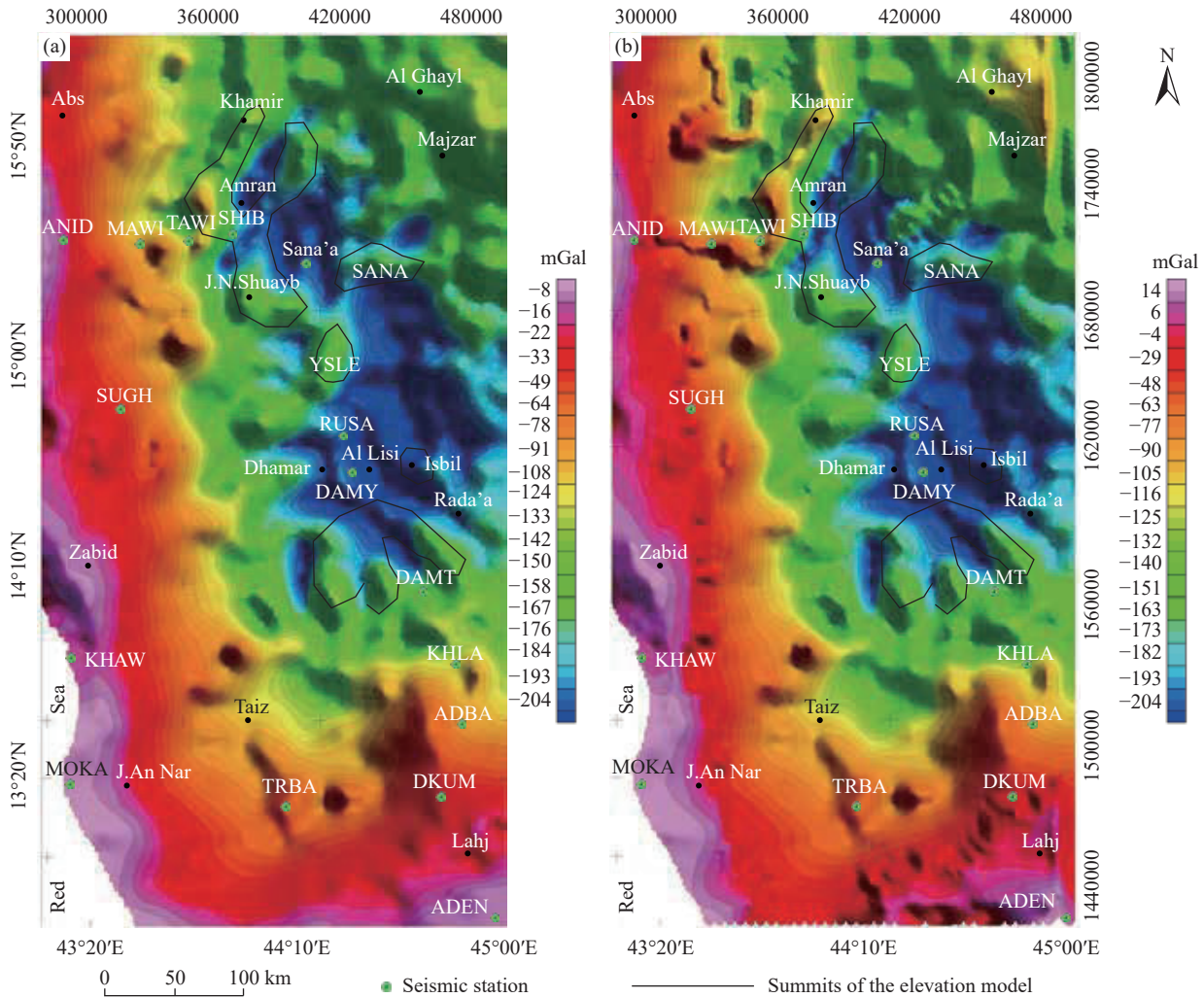


Fig. 2. Complete Bouguer gravity anomaly (a) and sediment corrected complete Bouguer gravity anomaly, SCCBA, (b).

$$F[\Delta g(x, y)] = -2\pi G \Delta \rho e^{-k|z_0|} \sum_{n=1}^{\infty} \frac{-|k|^{n-1}}{n!} F[\Delta \rho(x, y) h^n(x, y)], \quad (1)$$

Where $F[\Delta g(x, y)]$ is the Fourier transform of the gravity anomaly, G is the gravitational constant, $\Delta \rho$ is the density contrast across the interface, k is the wavenumber, and Z_0 is the mean depth of the interface from which the topographic variations are calculated.

The Parker-Oldenburg algorithm (Oldenburg DW, 1974) is used to compute the depth of the density discontinuity surface from gravity anomalies as follows:

$$F[h(x, y)] = -\frac{F[\Delta g(x, y)] e^{-k|z_0|}}{2\pi G \Delta \rho} - \sum_{n=2}^{\infty} \frac{|k|^{n-1}}{n!} F[h^n(x, y)] \quad (2)$$

This algorithm allows the determination of Moho discontinuity undulation by means of an iterative inversion scheme until a reasonable solution is reached. This procedure requires the mean Moho depth (Z_0) and the density contrast across the Moho discontinuity ($\Delta \rho$) to be predefined.

The Matlab code, “3DINVER.M” produced by Gomez-Ortiz D and Agarwal PN (2005), according to the Parker-

Oldenburg algorithm, is used in this study to calculate the Moho discontinuity depth. Gravity data are extended prior to the inversion to avoid aliasing and suppress ringing effects associated with the applications of the Fourier transform. Following Gomez-Ortiz D and Agarwal PN (2005), iteration stops after ten iterations or when the convergence criterion is satisfied (i.e., the “RMS” between Moho depths from the new and the previous iterations is equal to or less than 0.02 km).

Precise modelling of Moho interface undulation requires that the inverted gravity anomaly data be carefully filtered using critically selected cutoff wavelengths in order to remove both deep mantle and shallow crustal signals. Inversion results accuracy also depends on the used values of $\Delta \rho$ and Z_0 . Thus, to attain a more accurate image of Moho discontinuity, the Moho depth model of the study area was constructed in two steps.

3.2.1. Initial Moho depth models

Seventy-two initial models of Moho discontinuity depth are constructed during the first step of modelling by inverting the six sets of SCCBA data (i.e., the output of the six low pass filters applied to the SCCBA, Section 3.2.1.3) using different values of $\Delta \rho$, Z_0 in order to select the most appropriate values

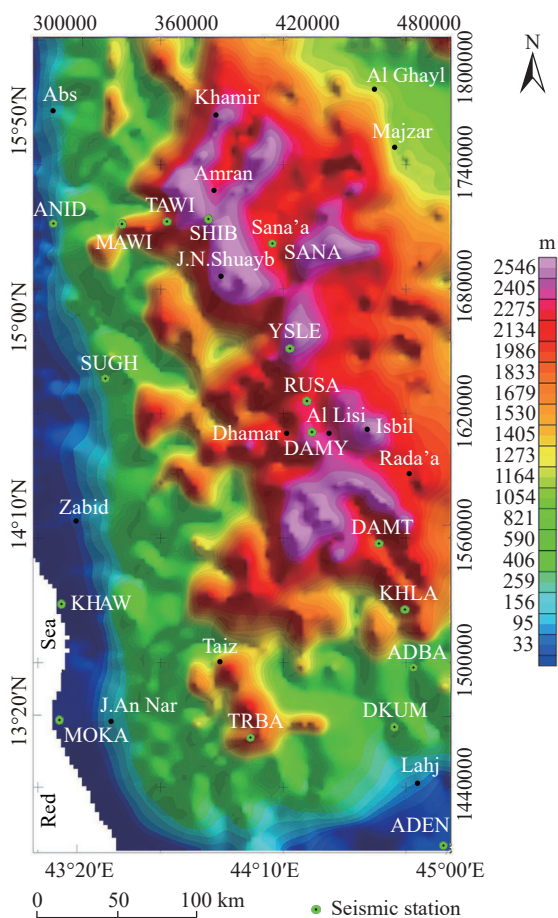


Fig. 3. Elevation model extracted from the global relief model Etopol (Modified from Amante C and Eakins BW, 2009).

of these parameters to create the final Moho depth model of the area. The tested range of $\Delta\rho$ and Z_0 was chosen based on earlier studies, as described in the next paragraphs.

3.2.1.1. Mean Moho depth (Z_0)

Earlier studies show variation in Moho discontinuity depth from less than 13–23 km below the Red Sea and the Gulf of Aden coasts to 35 km below the plateau (Egloff F et al., 1991; Makris J et al., 1991; Ahmed A et al., 2013). On the other side, the average depth of the Moho discontinuity estimated by Ahmed A et al. (2013) below 17 seismic stations distributed through the study area (Table 1, Figs. 1–4) is 28.2 km below sea level. Based on these studies, the tested Z_0 values in the first step of inversion are 23 km, 25 km, and 28 km.

3.2.1.2. Density contrast ($\Delta\rho$)

The average density of the crust (ρ_c) and mantle (ρ_m) in the study area is indirectly estimated from elastic wave velocity using the next empirical relation (Brocher TM, 2005);

$$\rho = 1.6612V_p - 0.4721V_p^2 + 0.0671V_p^3 - 0.0043V_p^4 + 0.000106V_p^5, \tag{3}$$

Where V_p is the velocity of compression (P) wave and ρ is the rock density.

Based on the average value of V_p in the upper mantle

Table 1. Crustal thickness in the study area obtained by receiver function analysis (Modified from Ahmed A et al., 2013).

Station name	Crustal thickness/km	Station elevation/km	Crustal thickness below sea level/km
ADEN	20.4	0.059	20.341
DKUM	23.6	0.397	23.203
ADBA	31	0.705	30.295
KHLA	33.8	1.457	32.343
DAMT	35.2	1.902	33.298
DAMY	35.2	2.46	32.74
RUSA	35.2	2.332	32.868
YSLE	35	2.557	32.443
SANA	35.4	2.253	33.147
SHIB	35.8	2.63	33.17
TAWI	32.2	2.333	29.867
MAWI	31.4	1.875	29.525
ANID	22.8	0.147	22.653
SUGH	23.2	0.248	22.952
KHAW	23	0.014	22.986
MOKA	21.5	0.029	21.471
TRBA	27.4	1.86	25.54

(7.95 km/s) and in the different crustal zones, except the sedimentary cover, (5 km/s, 6.2 km/s, 6.8 km/s, and 7 km/s) estimated from refraction experiments (see figure 8 of Egloff F et al., 1991), the crust-mantle density contrast ($\Delta\rho$) in the area is 0.48 g/cm³.

On the other side, the Moho depth model derived from gravity data in this work is constrained by the receiver function crustal thickness estimated below seventeen seismic stations distributed throughout the study area (Figs. 1–4) assuming an average crustal velocity (V_p) of 6.2 km/s (Ahmed A et al., 2013). This value and the above mentioned upper mantle V_p give $\Delta\rho$ of 0.50 g/cm³.

Both values of $\Delta\rho$ from equation (3), 0.48 g/cm³ & 0.50 g/cm³, seem to be high in view of the intensive magmatic activity that affected the study area in the form of intrusion and/or underplating (e.g., Ahmed A et al., 2013; Al Kadasi AN et al., 2020; Al Kadasi AN, 2021) which is expected to reduce the density contrast across the Moho boundary. Thus, the tested $\Delta\rho$ values in the initial step of modeling Moho undulations are 0.35 g/cm³, 0.40 g/cm³, 0.45 g/cm³ and 0.48 g/cm³.

3.2.1.3. Cutoff wavelength

Precise modeling of Moho undulations requires that the inverted gravity anomaly be only related to the Moho discontinuity. Several filters with different cutoff wavelengths were used in previous studies to prepare gravity data for inversion in order to obtain more stable models of Moho undulation (Tirel C et al., 2004; Gomez-Ortiz D and Agarwal BN, 2005; Shin YH et al., 2007).

In this work, due to the relatively small size of the study area, it is assumed that the SCCBA is free from deep mantle signals. On the other side, to ensure removing high frequency signals from the inverted gravity data, a Butterworth low-pass filter with six cutoff wavelengths (60 km, 90 km, 120 km, 150

Table 2. Initial Moho depth models obtained by inverting the filtered SCCBA data using six cutoff wavelengths and the RMS between the gravity and seismically derived Moho depths below 17 seismic stations distributed throughout the study area.

	No.	Z_0 /km	$\Delta\rho$ / g/cm ³	Moho depth/km		RMS /km		No.	Z_0 /km	$\Delta\rho$ /g/cm ³	Moho depth/km		RMS /km
				min.	Max.						min.	Max.	
Cutoff wavelength 60 km	1	23	0.35	13.14	36.93	3.159	Cutoff wavelength 150 km	37	23	0.35	13.32	36.6	2.614
	2		0.4	14.44	35.42	2.904		38		0.4	14.61	35.12	2.282
	3		0.45	15.44	34.2	2.910		39		0.45	15.6	33.98	2.297
	4		0.48	15.94	33.63	2.898		40		0.48	16.09	33.36	2.386
	5	25	0.35	14.55	39.79	3.154		41	25	0.35	14.75	39.47	2.992
	6		0.4	15.94	38.13	2.320		42		0.4	16.12	37.85	2.321
	7		0.45	17	36.85	1.898		43		0.45	17.17	36.6	1.590
	8		0.48	17.53	36.27	1.690		44		0.48	17.69	36.01	1.548
	9	28	0.35	16.57	44.11	5.030		45	28	0.35	16.82	43.82	5.473
	10		0.4	18.04	42.3	4.123		46		0.4	18.32	42.05	4.567
	11		0.45	19.17	40.93	3.517		47		0.45	19.47	40.7	3.981
	Cutoff wavelength 90 km	12		0.48	19.73	40.22		3.220	48		0.48	20.04	40
13		23	0.35	12.42	36.8	3.182	Cutoff wavelength 180 km	49	23	0.35	13.92	36.36	2.295
14			0.4	13.84	35.3	2.850		50		0.4	15.12	34.86	1.981
15			0.45	14.91	34.14	2.537		51		0.45	16.05	33.71	2.110
16			0.48	15.43	33.51	2.906		52		0.48	16.51	33.09	2.187
17		25	0.35	13.81	39.67	3.138		53	25	0.35	15.37	38.72	2.974
18			0.4	15.26	38.02	2.280		54		0.4	16.65	37.19	2.196
19			0.45	16.38	36.75	1.832		55		0.45	17.63	36.02	1.795
20			0.48	16.94	36.15	1.736		56		0.48	18.12	35.38	1.585
21		28	0.35	15.65	44	5.120		57	28	0.35	17.45	42.64	5.605
22			0.4	17.25	42.2	4.228		58		0.4	18.86	41.01	4.701
23			0.45	18.48	40.83	3.589		59		0.45	19.94	39.74	4.135
24		0.48	19.1	40.13	3.280	60			0.48	20.48	39.14	3.835	
Cutoff wavelength 120 km	25	23	0.35	12.63	36.79	2.967	Cutoff wavelength 210 km	61	23	0.35	14.28	36.25	2.074
	26		0.4	14.02	35.29	2.596		62		0.4	15.43	34.76	1.853
	27		0.45	14.89	34.3	2.571		63		0.45	16.32	33.61	2.005
	28		0.48	15.62	33.51	2.633		64		0.48	16.75	32.99	2.112
	29	25	0.35	14.05	39.66	3.110		65	25	0.35	15.71	38.59	2.951
	30		0.4	15.64	37.88	2.158		66		0.4	16.94	37.07	2.233
	31		0.45	16.44	36.98	1.700		67		0.45	17.89	35.9	1.882
	32		0.48	17.21	36.15	1.698		68		0.48	18.35	35.26	1.698
	33	28	0.35	16.08	43.99	5.341		69	28	0.35	17.76	42.19	5.409
	34		0.4	17.7	42.19	4.394		70		0.4	19.12	40.55	4.880
	35		0.45	18.92	40.83	3.797		71		0.45	20.16	39.28	4.414
	36		0.48	19.5	40.12	3.473		72		0.48	20.68	38.69	4.040

km, 180 km, and 210 km) is applied to the SCCBA. The output of these cutoff wavelengths is inverted using the above mentioned Z_0 and $\Delta\rho$ values in order to create initial Moho depth models.

The seventy-two initial Moho depth models obtained from the first step of inversion are compared with the seismically derived Moho depths under 17 seismic stations (Table 1, Figs. 1–4) and the root mean square error (RMS) between the two sets of Moho depths is calculated for each model. The parameters of the initial Moho depth models along with the calculated RMS are listed in (Table 2). This table indicates that model No. 44 (obtained by inverting the 150 km cutoff wavelength SCCBA using $Z_0=25$ km and $\Delta\rho=0.48$ g/cm³) gives the lowest RMS (1.55). Moho depth models obtained from the other five sets of SCCBA using $Z_0=25$ km and $\Delta\rho=0.48$ g/cm³ also show a small RMS compared with the other models from the same SCCBA data set. This suggests that the optimum Z_0

value is 25 km and the tested $\Delta\rho$ values in the second step of Moho depth modeling must be larger than 0.48 g/cm³.

3.2.2. Final Moho Depth model of the study area

Based on initial Moho depth models, the 150 km cutoff wavelength SCCBA data inverted to obtain the final Moho depth model of the study area using $Z_0=25$ km and $\Delta\rho$ of 0.50 g/cm³, 0.51 g/cm³, 0.52 g/cm³, 0.53 g/cm³ and 0.54 g/cm³. In order to further check the validity of using $Z_0=25$ km in calculating the final Moho depth model, Moho depths are also calculated using $Z_0=24$ km and 26 km.

The fifteen Moho depth models obtained in this step are also compared with the seismically derived Moho depths below 17 seismic stations in the study area and the root mean square error RMS between the two sets of Moho depths is calculated (Table 3).

3.3. Isostasy

To understand the relationship between Moho discontinuity undulation, ground surface topography, Bouguer gravity anomalies and isostasy, the isostatic gravity of the study area is calculated, following the Airy model, from the filtered topography of the area (i.e., the 150 km cutoff wavelength topographic data) using $Z_0=25$ km, $\rho_c=2.67$ g/cm³ and $\Delta\rho=0.5$ g/cm³, the same values used in calculating the final Moho depth model of the area. Isostatic anomalies/isostatic residuals of the study area are then obtained by subtracting isostatic gravity from Bouguer gravity.

Table 3. Moho depth models obtained by inverting of 150 km cutoff wavelength SCCBA data and the RMS between the gravity and seismically derived Moho depths below 17 seismic stations distributed throughout the study area.

Model No.	Z_0 /km	$\Delta\rho$ /g/cm ³	Moho depth/km		RMS/km
			Min.	Max.	
1	24	0.5	17.19	34.29	1.69
2		0.51	17.34	34.11	1.73
3		0.52	17.47	33.93	1.83
4		0.53	17.6	33.76	1.85
5		0.54	17.72	33.59	1.87
6	25	0.5	18	35.61	1.34
7		0.51	18.15	35.42	1.36
8		0.52	18.29	35.24	1.41
9		0.53	18.42	35.06	1.42
10		0.54	18.55	34.89	1.44
11	26	0.5	18.8	36.94	1.77
12		0.51	18.95	36.75	1.59
13		0.52	19.1	36.56	1.62
14		0.53	19.23	36.38	1.62
15		0.54	19.36	36.2	1.64

4. Results and discussion

4.1. Sediment corrected complete Bouguer anomaly (SCCBA) map

The general features of gravity anomalies shown in Fig. 2b are briefly described in this section. The gravity anomaly is gradually decreasing from about 20 mGal over coastal regions to -210 mGal over the plateau, indicating gradual crustal thickening from the Red Sea and the Gulf of Aden ridges toward the plateau. The transition from coastal regions to the plateau shows a steep gradient in the gravity field (more clearly seen along the Red Sea coastal plain), marking the sudden increase in the Great Escarpment elevation from about 200 m to 1000 m.

A general anticorrelation is clearly observed between the SCCBA (Figs. 2a–b) and ground surface topography (Fig. 3), but a closer inspection indicates that topographic feature peaks are slightly shifted away from gravity anomaly minima. This suggests another factor also contributed to the observed gravity anomalies, along with crustal thickening.

The minimal gravity anomaly belt running between Sana'a-Amran and Dhamar-Rada'a Quaternary volcanic fields (Figs. 1, 2, 4) coincides well with the upper mantle low velocity anomaly zone attributed to hot mantle upwellings (Korostelev F et al., 2014). As the cutoff wavelength of the low pass filter applied to the SCCBA increases from 60 km to 210 km (section 3.2.1), the negative anomaly peak beneath the Sana'a-Amran region gradually diminishes (Figs. 4a–c), indicating a relatively small size of this hot mantle upwelling. Furthermore, the minimal gravity anomaly belt becomes more localized between Sana'a and Damt with its peak situated below/around the Al Lisi and Isbil active volcanoes in the Dhamar-Rada'a Quaternary volcanic field (Figs. 4a–c).

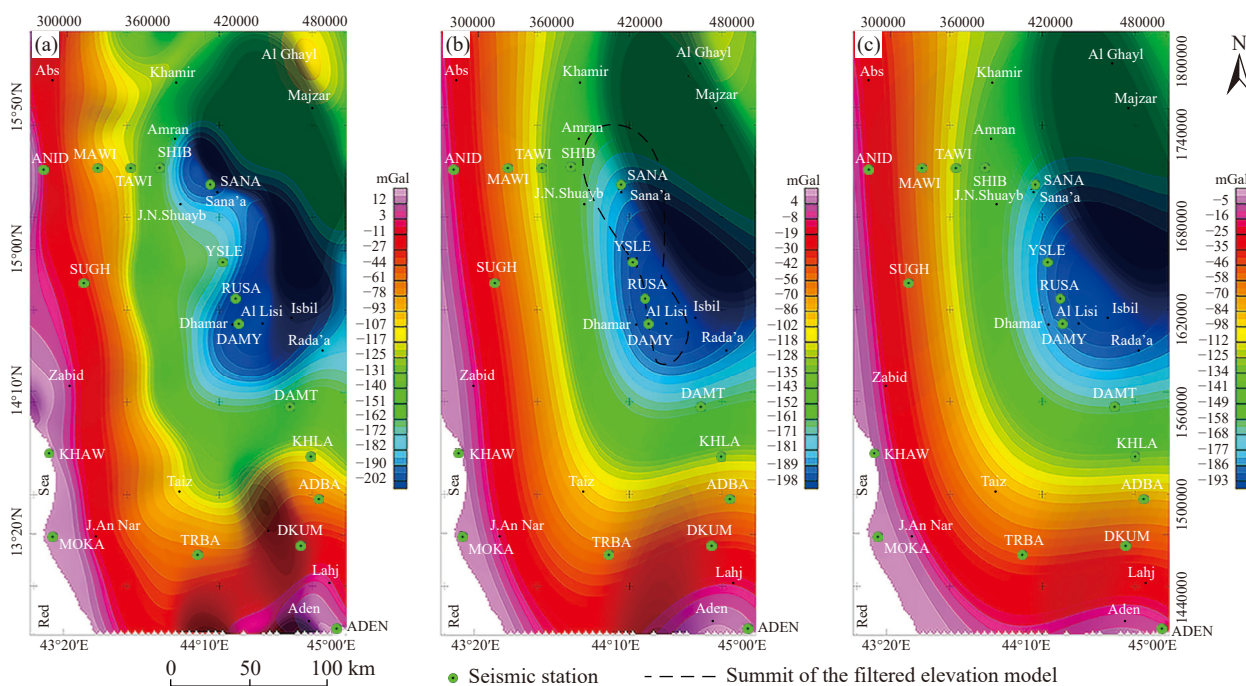


Fig. 4. Sediment corrected complete Bouguer anomaly (SCCBA) with cutoff wavelengths of 60 km (a), 150 km (b), and 210 km (c).

The reactivation of deep crustal faults attributed to the final stage of the Pan African Orogeny during the Cenozoic assists upper mantle decompression melting and provides magma for Cenozoic volcanic activity (Al Kadasi AN, 2021; Sanfilippo A et al., 2021). This indicates that, in addition to crustal thickening, hot magmatic materials also contributed to the gravity anomaly belt below the highlands (Figs. 2, 4) which explains the mismatch between the gravity anomaly minima and topographic feature peaks (Fig. 2). Several studies delineated mantle anomaly zones under the study area (e.g., Chang SJ and Lee SV, 2011; Chang SJ et al., 2011; Corbeau J et al., 2014). Similarly, Daradich A et al. (2003) indicated an elongated upper mantle low velocity zone beneath the Arabian shield. Park Y et al. (2007) delineated a NW-SE trending mantle anomaly zone below the Arabian shield associated with the Cenozoic uplift and volcanic centres on the shield. Lim JA et al. (2020) found an elongated, narrow, low-velocity anomaly below the Arabian shield that was connected to the asthenospheric flow from the Afar plume. Mukhopadhyay M et al. (2021) imaged a 10 to 12 km thick and 40 km wide uplifted upper mantle zone beneath the Tihamat plain, SW- Saudi Arabia, at depths varying between 37 km and 45 km.

4.2. Moho depth model of the study area

Table 3 shows 15 Moho depth models obtained by inverting the 150 km cutoff wavelength SCCBA (section 3.2.2.). Among these models, model No. 6 (with $Z_0=25$ km and $\Delta\rho=0.50$ g/cm³) gives the lowest RMS (1.34) between the seismically derived and the gravity-derived Moho depths under 17 seismic stations in the study area. Thus, this model (model No. 6, Fig. 5) reflects the most accurate image of Moho discontinuity undulation in the study area. Moreover, the difference in the RMS values of the different models listed in Table 3 is quite small, which confirms the stability of the estimated Moho depths.

Three zones of Moho depth can be easily recognized on the 3D Moho depth model of the study area (Fig. 5). The shallow zone is located at depths varying between 20 km and 24 km below the Red Sea and the Gulf of Aden coastal plains, and the intermediate zone lies at depths of 24 km to 30 km beneath the transitional region between the coastal plains and the plateau. The deep zone is located beneath the plateau at depths vary between 30 km to 35 km and its deepest part is largely coincident with the Dhamar-Rada Quaternary volcanic field.

Moho depths from this study agreed well with Makris J et al. (1991) who recorded an average crustal thickness of 35 km below the Sana'a region and 22 km below the Tihama plain. The obtained Moho depths also agreed well with crustal thickness from the receiver function, which varies from 20 km to 23 km under coastal regions to 35 km below the plateau (Ahmed A et al., 2013). Furthermore, Moho depths from the present work also lying within the range of the estimated Moho depths below the Arabian plate by earlier regional and semi-regional studies such as Gettings ME et al. (1986) 20 km

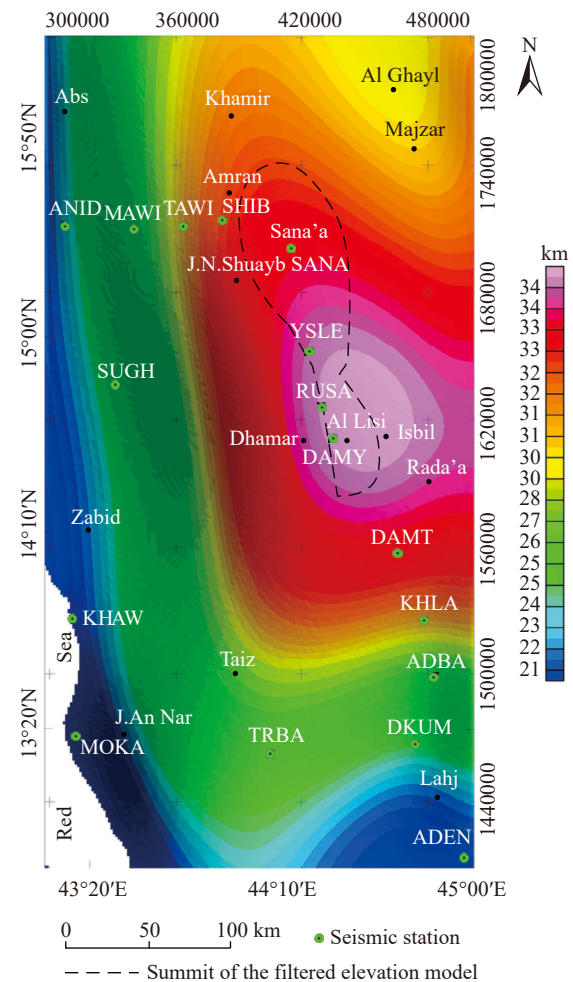


Fig. 5. The three dimensional Moho depth model constructed in this study from EGM2008 based on the Parker-Oldenburg algorithm.

to 40 km, Chang SJ and Lee SV (2011) 25 km to 35 km, Mechie J et al. (2013) 30 km to 45 km, Gvirtzman Z et al. (2016) 20 km to 45 km, and by Al Amri A et al. (2017) 20 km to 25 km near the Red Sea coasts.

The calculated gravity anomaly from the Moho depth model of the study area (Fig. 6a) is very close to the observed gravity anomaly (Fig. 4b) and the difference between them (gravity residuals) varies from -7 mGal to 9 mGal (Fig. 6b). These residuals are mainly attributed to the assumed constant $\Delta\rho$ across the Moho interface by the Parker-Oldenburg algorithm (Oldenburg DW, 1974), which causes a local decrease in the calculated gravity field (relative to the observed field) in regions characterized by a higher $\Delta\rho$ value than that used in inverting gravity data, and vice versa.

Two negative belts are clearly identified on the gravity residual map (Fig. 6b). The first one, running between the Dhamar-Rada'a and Sana'a-Amran Quaternary volcanic fields coincides with the upper mantle low velocity zone imaged by Korostelev F et al. (2014). The second belt extends between the Dhamar-Rada'a volcanic field and the Late Miocene Jabal An Nar volcanic area, on the Red Sea coast, where an upper and lower mantle velocity anomalies attributed to the Afar mantle plume are also imaged by Korostelev F et al. (2014) from the surface to a depth of 300 km. Similar to the first belt

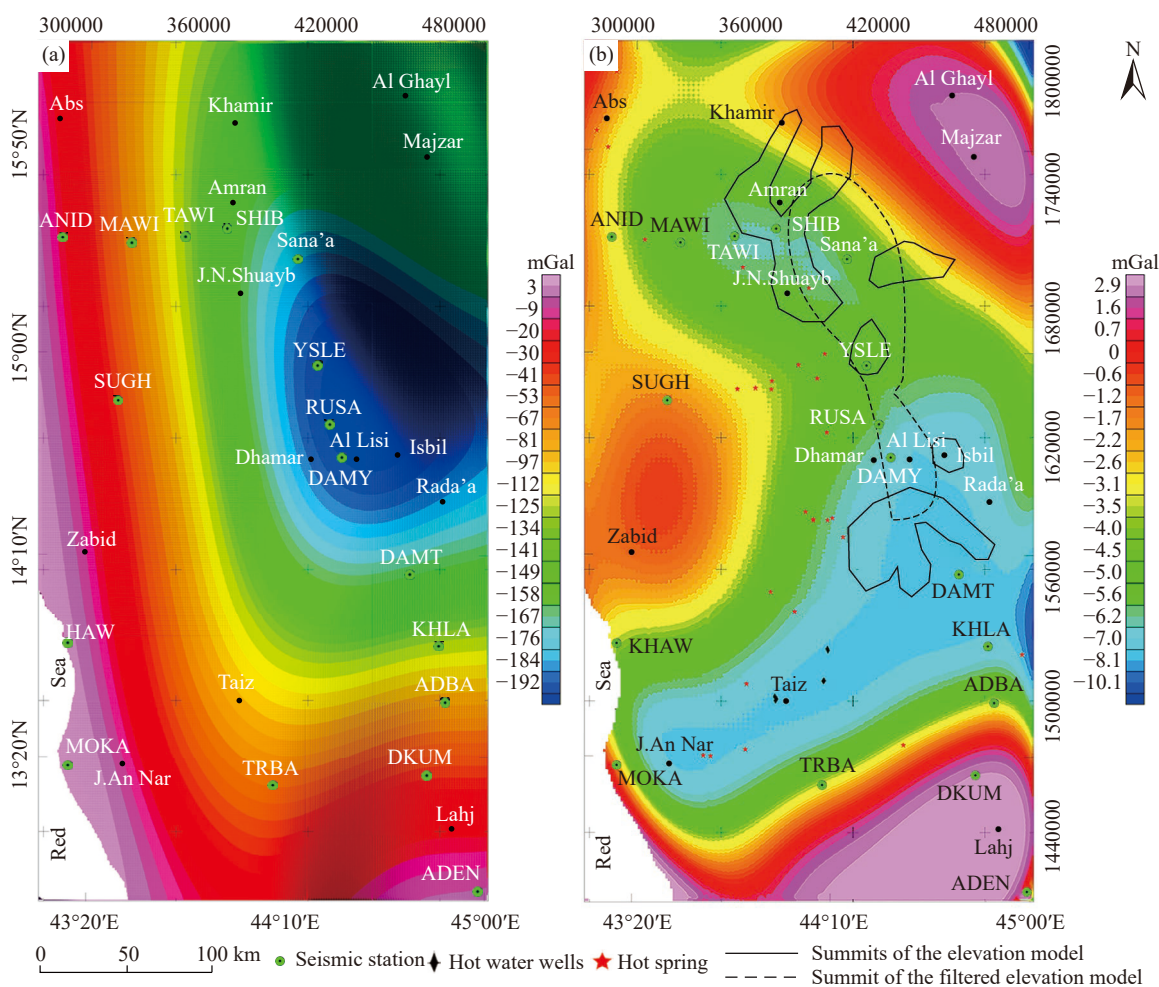


Fig. 6. The calculated gravity anomaly from the constructed Moho depth model of the study area (a) and the difference (gravity residuals) between the observed and the calculated gravity anomalies (b).

of gravity residuals, the second belt suggests a channel of hot magmatic materials (or a linear arrangement of small, isolated mantle upwellings) extends along this region.

Several evidences from earlier studies support this interpretation such as the widespread geothermal activity, with a clear mantle imprint distributed along these channels (Fig. 6b) in the form of fumaroles, boiling pools, hot springs, hot groundwater wells, etc (Minissale A et al., 2007). Isotopic data show that the Late Miocene volcanic activity in Southwestern Arabia was shifted northeastward in response to the dispersion of the Afar plume head and partially overlapped during the Quaternary (Orihashi Y et al., 1998). The interpreted magmatic channels in this work, based on the negative gravity residuals, also coincide with the narrow low velocity zone attributed to an asthenospheric flow from the Afar plume extending from Afar depression to Harrats Ithnayn and Lunayyir, Western Arabia (Figs 8, 9 of Lim JA et al., 2020). Furthermore, a northeastward dispersion of the Afar mantle plume has been imaged beneath the Arabian plate by several earlier studies (such as Chang SJ and Lee SV, 2011; Chang SJ et al., 2011; Kaviani A et al., 2020).

On the other side, a positive closure of gravity residuals is shown in the southern part of Fig. 6b, matching the Gulf of Aden coastal plain and the southern basement block (Fig. 1).

This region is highly intruded by high density materials (Davison I et al., 1994, 1998; Ahmed A et al., 2013; Ali MY and Watts AB, 2013) which increase crustal density and consequently increase the observed gravity anomaly relative to the calculated gravity anomaly. The weak Moho Ps conversion phase from DKUM and ADEN seismic stations indicated by Ahmed A et al. (2013) confirm the reduction of density contrast across the Moho interface in this region and assists this interpretation. The same explanation is also valid for the relatively low amplitude positive closure at the upper eastern corner of Fig. 6b which is located between Sana'a-Amran and Marib-Sirwah Quaternary volcanic fields, correlated with the Al Jawf graben boundary, and associated at the surface, in addition to the limestone with crystalline basement, granite and other intrusive bodies.

4.3. Isostasy

Isostatically compensated regions are generally characterized by zero or very low isostatic anomalies, whereas overcompensated and undercompensated regions reflect negative and positive anomalies, respectively. This is because both the Bouguer gravity anomaly and the isostatic gravity anomaly are negative, but the Bouguer gravity anomaly is

numerically larger than the isostatic gravity anomaly in overcompensated regions and smaller in undercompensated regions.

Isostatic anomaly in the study area (Fig. 7) indicates that undercompensated regions (isostatic residuals > 9 mGal) occupied the western and southern parts of the area correlated with coastal plains and the transitional zone between coastal plains and the plateau, mostly matching the shallow and intermediate zones on the Moho depth model (Fig. 5). In these regions, the crust is gradually thinned seaward, stretched, and intruded and/or underplated by high density materials mostly of mantle origin (Davison I et al., 1994, 1998; Ahmed A et al., 2013; Ali MY and Watts AB, 2013; Korostelev F et al., 2014; Lim JA et al., 2020), which explain the deepening of isostatic Moho relative to gravity Moho in these regions.

The plateau shows a couple of compensated and overcompensated conditions. Isostatically compensated region (with isostatic residuals between -9 mGal to 9 mGal) occupied a larger part of the plateau. While the overcompensated region (isostatic residuals < -9 mGal) forming an irregular spot matching well the deepest part of the Moho depth model (Fig. 5) below Dhamar-Rada'a Quaternary volcanic field. This suggests that the thermal

activity and the erupted magmatic materials in this region reduced the density of the deep lithosphere and asthenosphere and contributed to the deepening of gravity Moho relative to isostatic Moho.

The above discussion suggests that the overall isostatic balance of the area (indicated by the general anticorrelation between ground surface topography and both Bouguer anomalies and the Moho depth model) is achieved by a cooperative effect of several mechanisms (crustal thickening, buoyancy, mantle upwelling, and magmatic activity).

Crustal thickening is generally caused by lithosphere shortening and/or magmatism (volcanism and underplating). In the study area, a huge amount of mantle-derived magma erupted throughout the plateau during the Oligo-Miocene and continued in the Quaternary due to the effect of the Afar mantle plume. (Menzies MA et al., 1992, 1997; Davison I et al., 1994; Baker J et al., 1996). Isotopic data reflect that flood and intraplate basalts are partially derived from garnet-facies mantle melt (Baker J, 1996; Ali MY and Watts AB, 2013; Furman T et al., 2016), suggesting that the lower part of the lithosphere is thinned and permits the ascending of the hot plume/asthenosphere to the upper part of the mantle and undergo decompression melting (Davison I et al., 1998). Thinning of the cold lithosphere drives surface uplift (Davison I et al., 1998; Lim JA et al., 2020), while decompression melting of the hot asthenosphere leads to basaltic underplating (Ji WQ et al., 2012).

As indicated in Section (1), the average elevation of the Yemeni highlands is 2200 m ASL. Of this, the volcanic activity increased the surface elevation by 600 m and the remaining height is attributed to lithospheric thinning, buoyancy, magmatic underplating and flexural upwarp (Davison I et al., 1998).

5. Conclusions

(i) A three-dimensional Moho depth model of the study area is constructed by inverting gravity data from the EGM2008 using the Parker-Oldenburg algorithm. Three zones of Moho depth are recognized on this model. The shallow zone lies below the Red Sea and the Gulf of Aden coastal plains at depths of 20 km to 24 km; the intermediate zone is situated at depths of 24 km to 30 km (correlated mostly with the transitional zone to the plateau); and the deep zone lies below the plateau at depths ranging from 30 km to 35 km. The deepest part of the Moho discontinuity coincides mainly with the Dhamar-Rada'a Quaternary volcanic field.

(ii) The difference between the calculated gravity anomalies from the Moho depth model of the study area and the observed gravity anomalies pointing to two channels of hot magmatic materials linked the Dhamar-Rada'a Quaternary volcanic field with the Sana'a-Amran Quaternary volcanic field, on one side, and with the Late Miocene Jabal An Nar volcanic area, on the other side. The upper mantle low velocity anomaly zones and the widespread geothermal activity recorded by earlier studies in these regions support this conclusion.

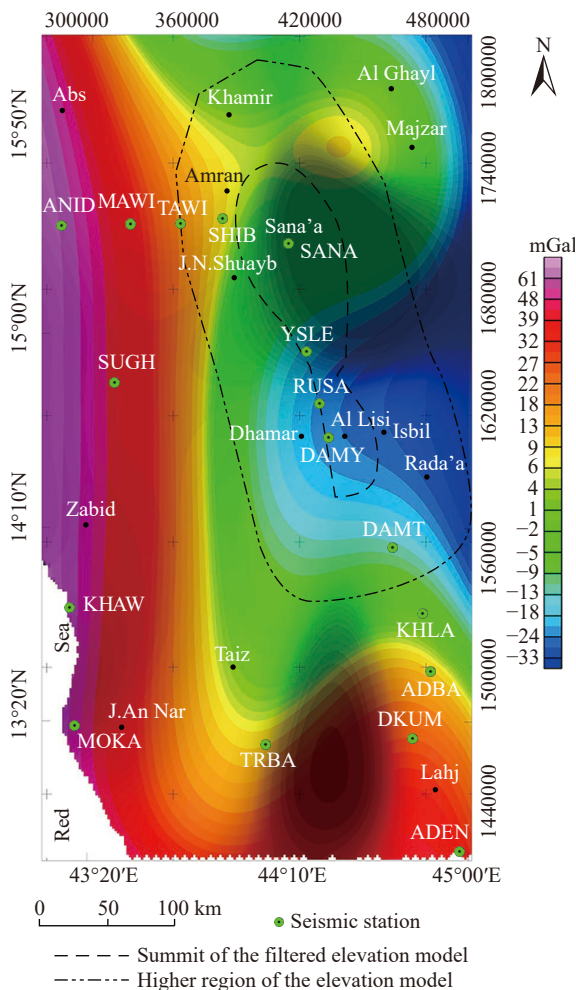


Fig. 7. The isostatic anomaly model of the area calculated according to the Airy model for isostatic compensation.

(iii) Several mechanisms (such as uplift, magmatism, buoyancy, and mantle upwelling) are contribute to the overall isostatic balance of the study area.

Declaration of competing interest

The author declares no conflicts of interest.

Acknowledgments

Deep thanks to the two anonymous reviewers for their valuable comments and suggestions to improve this manuscript, as well as for future work. The author is greatly thankful for the help of the China Geology editors in processing this manuscript and producing it in this form. The gravity data used in this study was obtained from the EGM2008 provided by the International Centre for Global Earth Models (ICGEM), special thanks to this organization.

References

- Ahmed A, Tiberi C, Leroy S, Stuart GW, Keir D, Sholan J, Khanbari K, Al-Ganad I, Basuyau C. 2013. Crustal structure of the rifted volcanic margins and uplifted plateau of Western Yemen from receiver function analysis. *Geophysical Journal International*, 193, 1673–1690. doi: [10.1093/gji/ggt072](https://doi.org/10.1093/gji/ggt072).
- Al-Amri A, Abdelrahman K, Andreae MO, Al-Dabbagh M. 2017. Crustal and upper mantle structures beneath the Arabian Shield and Red Sea. In: Roure F.; Amin AA; Khomsi S; Al Garni MAM. (eds.), *Lithosphere Dynamics and Sedimentary Basins of the Arabian Plate and Surrounding Areas*, *Frontiers in Earth Sciences*. Switzerland, Springer Nature, 3-29. doi: [10.1007/978-3-319-44726-1_1](https://doi.org/10.1007/978-3-319-44726-1_1).
- Ali MY, Watts AB. 2013. Subsidence history, crustal structure, and evolution of the Somaliland -Yemen conjugate margin. *Journal of Geophysical Research: Solid Earth*, 118, 1638–1649. doi: [10.1002/jgrb.50113](https://doi.org/10.1002/jgrb.50113).
- Al Kadasi AN, A-Aydrus AA, Mustafa MS. 2020. Estimation of Curie point depth in southwestern Yemen from spectral analysis of aeromagnetic data. *Arabian Journal of Geosciences*, 13(5), 1–14. doi: [10.1007/s12517-020-5196-0](https://doi.org/10.1007/s12517-020-5196-0).
- Al Kadasi AN. 2021. Geologic implications of aeromagnetic data over the volcanic plateau, Western Yemen. *Taiz University Research Journal*, 28, 30–49.
- Alsinawi SA, Al Aydrus AA. 1999. *Seismicity of Yemen*. Sana'a, Obadi Studies and Publishing Center, 1–297.
- Ambraseys NN, Melville CP. 1983. Seismicity of Yemen. *Nature*, 303, 321–323. doi: [10.1038/303321a0](https://doi.org/10.1038/303321a0).
- Ambraseys NN, Melville CP, Adams RD. 1994. *The Seismicity of Egypt, Arabia and the Red Sea: A Historic Review*. New York, Cambridge University Press, 1–181.
- Amante C, Eakins BW. 2009. ETOPO1 Arc-minute global relief model: procedures, data sources and analysis, NOAA Technical Memorandum NESDIS NGDC-24, 19 pp., NOAA, Silver Spring, Md.
- Arabelos DN, Tscherning CC. 2010. A comparison of recent earth gravitational models with emphasis on their contribution in refining the gravity and geoid at continental or regional scale. *Journal of Geodesy*, 84, 643–660. doi: [10.1007/s00190-010-0397-z](https://doi.org/10.1007/s00190-010-0397-z).
- Baker J, Snee L, Menzies M. 1996. A brief Oligocene period of flood volcanism in Yemen: implications for duration and rate of continental flood volcanism at the Afro-Arabian triple junction. *Earth Planetary Science Letters*, 138, 39–55. doi: [10.1016/0012-821X\(95\)00229-6](https://doi.org/10.1016/0012-821X(95)00229-6).
- Bassin CG, Laske G, Masters G. 2000. The current limits of resolution for surface wave tomography in North America, *EOS Transactions. American Geophysical Union*, 81(48), F897.
- Brocher TM. 2005. Empirical relations between elastic wave speeds and density in the earth's crust. *Bulletin of the Seismological Society of America*, 95(6), 2081–2092. doi: [10.1785/0120050077](https://doi.org/10.1785/0120050077).
- Capaldi G, Chiesa S, Manetti P, Orsi G, Poli G. 1987. Tertiary anorogenic granites of the western border of the Yemen Plateau. *Lithos*, 20(6), 433–444. doi: [10.1016/0024-4937\(87\)90028-4](https://doi.org/10.1016/0024-4937(87)90028-4).
- Chang SJ, Lee SV. 2011. Mantle plumes and associated flow beneath Arabia and East Africa. *Earth Planetary Science Letters*, 302, 448–454. doi: [10.1016/j.epsl.2010.12.050](https://doi.org/10.1016/j.epsl.2010.12.050).
- Chang SJ, Merino G, Lee SV, Stein S, Stein CA. 2011. Mantle flow beneath Arabia offset from the opening Red Sea. *Geophysical Research Letters*, 38, L04301. doi: [10.1029/2010GL045852](https://doi.org/10.1029/2010GL045852).
- Chazot V, Menzies MA, Baker J. 1998. Pre-, syn- and post-rift volcanism on the margin of the Arabian Plate. In: Purser B. H. and Bosence D. W. J. (eds), *Sedimentation and Tectonics of Rift Basins: Red Sea-Gulf of Aden*. London, Chapman & Hall, 50–55.
- Chiesa S, La Volpe L, Lirer L, Orsi G. 1983. Geological and structural outline of Yemen Plateau, Yemen Arab Republic. *Neues Jahrbuch für Geologie und Paläontologie-Monatshefte*, 11, 641–656.
- Chiesa S, Civetta L, De Fino M, La Volpe L, Orsi G. 1989. The Yemen trap series: genesis and evolution of a continental flood basalt province. *Journal of Volcanology and Geothermal Research*, 36, 337–350. doi: [10.1016/0377-0273\(89\)90078-4](https://doi.org/10.1016/0377-0273(89)90078-4).
- Civetta L, Lavolpe L, Lirer L. 1978. K-Ar ages of the Yemen Plateau. *Journal of Volcanology and Geothermal Research*, 4, 307–314. doi: [10.1016/0377-0273\(78\)90019-7](https://doi.org/10.1016/0377-0273(78)90019-7).
- Corbeau J, Rolandone F, Leory S, Al-Lazki A, Stork AL, Kier D, Stuart GW, Hammond JO, Doubre C, Vergne J, Ahmed A, Khanbari K. 2014. Uppermost mantle velocity from Pn tomography in the Gulf of Aden. *Geosphere*, 10(5), 958–968. doi: [10.1130/GES01052.1](https://doi.org/10.1130/GES01052.1).
- Daradich A, Mitrovica JX, Pysklywec RN, Willett SD, Forte AM. 2003. Mantle flow, dynamic topography, and rift-flank uplift of Arabia. *Geology*, 31, 901–904.
- Davidson I, Al-Kadasi M, Al-Khribash S, Al-Subbary A, Baker J, Blaky S, Bosence D, Dart C, Heaton R, McClay K, Menzies M, Nichols L, Owen L, Yelland A. 1994. Geological evolution of the southern Red Sea rift margin: Republic of Yemen. *Geological Society of America Bulletin*, 106, 1474–1493. doi: [10.1130/0016-7606\(1994\)106<1474:GEOTSR>2.3.CO;2](https://doi.org/10.1130/0016-7606(1994)106<1474:GEOTSR>2.3.CO;2).
- Davidson I, Tatnell MR, Owen LA, Jenkins G, Baker J. 1998. Tectonic geomorphology and rates of crustal processes along the Red Sea margin, north-west Yemen. In: Purser B. H. and Bosence D. W. J. (eds), *Sedimentation and Tectonics of Rift Basins: Red Sea-Gulf of Aden*. London, Chapman & Hall, 595–612.
- Egloff F, Rhim R, Makris J, Izzeldin YA, Bobsien M, Meier K, Junge P, Noman T, Warsi W. 1991. Contrasting structural styles of the eastern and western margins of the southern Red Sea: the 1988 SONNE experiment. *Tectonophysics*, 198, 329–353. doi: [10.1016/0040-1951\(91\)90159-P](https://doi.org/10.1016/0040-1951(91)90159-P).
- Evariste NH, Genyoul L, Tahod TC, Joseph K, Severin N, Tiedeu A, Xiaoping KE. 2014. Crustal structure beneath Cameroon from EGM2008. *Geodesy and Geodyoamics*, 5(1), 1–10. doi: [10.3724/SP.J.1246.2014.01001](https://doi.org/10.3724/SP.J.1246.2014.01001).
- Furman T, Nelson WR, Elkins-Tanton LT. 2016. Evolution of the East African Rift: Drip magmatism, lithospheric thinning and Mafic Volcanism. *Geochimica et Cosmochimica Acta*, 185, 418–434. doi: [10.1016/j.gca.2016.03.024](https://doi.org/10.1016/j.gca.2016.03.024).
- Gettings ME, Blank H, Mooney WD, Healey JH. 1986. Crustal structure of Southwestern Saudi Arabia. *Journal of Geophysical Research*, 91(B6), 6491–6512. doi: [10.1029/JB091iB06p06491](https://doi.org/10.1029/JB091iB06p06491).
- Gómez-Ortiz D., Agarwal BNP. 2005. 3DINVER. M:A matlab program to invert the gravity anomaly over a 3D horizontal density interface by Parker-Oldenburg's algorithm. *Computers & Geosciences*, 31, 513–520.
- Guy A, Holzrichter N., Ebbing J. 2017. Moho depth model for the Central Asian Orogenic Belt from satellite gravity gradients. *American Geophysical Union*, 122, 7388–7407. doi: [10.1002/2017JB014120](https://doi.org/10.1002/2017JB014120).
- Gvirtzman Z, Faccenna C, Becker TW. 2016. Isostasy, flexure, and

- dynamic topography. *Tectonophysics*, 683, 255–271. doi: [10.1016/j.tecto.2016.05.041](https://doi.org/10.1016/j.tecto.2016.05.041).
- Huchon P, Jestin F, Cantagrel JM, Gaulier JM, Al-Khribash S, Gafaneh A. 1991. Extensional deformations in Yemen since Oligocene and the Afar triple junction. *Annales Tectonicae*, 5, 141–163.
- Ji WQ, Wu FY, Liu CZ, Chung SL. 2012. Early Eocene crustal thickening in southern Tibet: New age and geochemical constraints from the Gangdese batholiths. *Journal of Asian Earth Sciences*, 53, 82–95. doi: [10.1016/j.jseae.2011.08.020](https://doi.org/10.1016/j.jseae.2011.08.020).
- Kaviani A, Paul A, Moradi A, Mai PM, Pilia S, Boschi L, Rumpker G, Lu Y, Tang Z, Sandvol E. 2020. Crustal and uppermost mantle shear wave velocity structure beneath the Middle East from surface wave tomography. *Geophysical Journal International*, 221, 1349–1365. doi: [10.1093/gji/ggaa075](https://doi.org/10.1093/gji/ggaa075).
- Korostelev F, Basuyau C, Leroy S, Tiber C, Ahmed A, Stuart GW, Keir D, Rolandone F, Al Ganad I, Khanbari K, Boschi L. 2014. Crustal and upper mantle structure beneath south-western margin of the Arabian Peninsula from teleseismic tomography. *Geochemistry Geophysics Geosystems*, 15, 2850–2864. doi: [10.1002/2014GC005316](https://doi.org/10.1002/2014GC005316).
- Laske G, Masters G, Ma Z, Pasyanos M. 2013. Update on CRUST1.0 - A 1-degree global Model of earth's crust. *Geophysical Research Abstracts*, 15, Abstract EGU2013-2658.
- Lemenkova P. 2021. Seismicity in Yemen and the Gulf of Aden in a geological context. *Riscurisi Catastrofe*, An XXI, 28 (NR. 1), 43–57.
- Levin G, Park J. 2000. Shear zones in Proterozoic lithosphere of the Arabian shield and the nature of the Hali's discontinuity. *Tectonophysics*, 323, 131–143. doi: [10.1016/S0040-1951\(00\)00105-0](https://doi.org/10.1016/S0040-1951(00)00105-0).
- Lim JA, Chang SJ, Mai PM, Zahran H. 2020. Asthenospheric flow of plume material beneath Arabia inferred from S-wave travel-time tomography. *Journal of Geophysical Research: Solid Earth*, 125, e2020JB019666. doi: [10.1029/2020jb019666](https://doi.org/10.1029/2020jb019666).
- Makris J, Henke CH, Egloff F, Akamaluk T. 1991. The gravity field of the Red Sea and East Africa. *Tectonophysics*, 198, 369–381. doi: [10.1016/0040-1951\(91\)90161-K](https://doi.org/10.1016/0040-1951(91)90161-K).
- Manetti P, Capaldi G, Chiesa S, Civetta L, Conticelli S, Gasparon M, Volpe LL, Orsi G. 1991. Magmatism of the eastern Red Sea margin in the northern part of Yemen from Oligocene to Present. *Tectonophysics*, 198, 181–202.
- McCombe DA, Fernete GL, Alawi, AI. 1994. The geological and mineral resources of Yemen. Ministry of Oil and Mineral Resources, Geological Survey and Minerals Board, Yemen Mineral Sector Project, Technical Report.
- Mechie J, Ben-Avraham Z, Weber MH, Götze H, Koulakov I, Mohsen A, Stiller M. 2013. The distribution of Moho depths beneath the Arabian plate and margins. *Tectonophysics*, 609, 234–249. doi: [10.1016/j.tecto.2012.11.015](https://doi.org/10.1016/j.tecto.2012.11.015).
- Meliani O, Bourmatte A, Hamoudi M, Haddoum H, Quesnel Y. 2016. Moho depth derived from gravity and magnetic data in the Southern Atlas Flexure (Algeria). *Journal of African Earth Sciences*, 121, 100–107. doi: [10.1016/j.jafrearsci.2016.05.017](https://doi.org/10.1016/j.jafrearsci.2016.05.017).
- Menzies MA., Baker J., Bosence D., Dart E., Davison I. et al., 1992. The timing of magmatism, uplift and crustal extension - preliminary observations from Yemen. In: Storey B. (ed.), *Magmatism and Continental Breakup*. Geological Society of London, Special publication, 68, 293–304.
- Menzies MA, Baker J, Chazot G, Al-Kadasi M. 1997. Evolution of the Red Sea volcanic margin, western Yemen. In Mahoney J. J. and Coffin M. F. (eds), *Large Igneous Provinces: Continental, Oceanic and Planetary Flood Volcanism*. Geophysical Monograph, 100, American Geophysical Union, 29–43. doi: [10.1029/GM100p0029](https://doi.org/10.1029/GM100p0029).
- Minissale A, Mattash MA, Vaselli O, Tassi F, Al-Ganad IN, Selmo E, Nasr MS, Tedesco D, Poreda R, Ad-Dukhain AM, Hazzae MK. 2007. Thermal springs, fumaroles and gas vents of continental Yemen: their relation with active tectonics, regional hydrology and the country's geothermal potential. *Applied Geochemistry*, 22, 799–820. doi: [10.1016/j.apgeochem.2006.11.009](https://doi.org/10.1016/j.apgeochem.2006.11.009).
- Mukhopadhyay M, Mukhopadhyay B, Elawadi VE, Durga VK, Al-Arif N. 2021. Crustal structure beneath the volcanic field in the Tihamat Plains, Saudi Arabia: an integrated model constrained by gravity modelling and receiver function results. *Journal of Asian Earth Sciences*, 206, 104614. doi: [10.1016/j.jseae.2020.104614](https://doi.org/10.1016/j.jseae.2020.104614).
- Nehlig P, Genna A, Asfirane F. 2002. A review of the Pan-African evolution of the Arabian shield. *GeoArabia*, 7, 103–124. doi: [10.2113/geoarabia0701103](https://doi.org/10.2113/geoarabia0701103).
- Oldenburg DW. 1974. The inversion and interpretation of gravity anomalies. *Geophysics*, 39, 526–536. doi: [10.1190/1.1440444](https://doi.org/10.1190/1.1440444).
- Orihashi Y, Al-Jailani A, Naga K. 1998. Dispersion of the Afar plume: implications from the spatiotemporal distribution of the Late Miocene to Recent Volcanics, Southwestern Arabian Peninsula. *Gondwana Research*, 1(2), 221–234. doi: [10.1016/S1342-937X\(05\)70833-9](https://doi.org/10.1016/S1342-937X(05)70833-9).
- Park Y, Nyblade AA, Rodgers AJ, Al-Amri A. 2007. Upper mantle structure beneath the Arabian Peninsula and Northern Red Sea from teleseismic body wave tomography: Implications for the origin of Cenozoic uplift and volcanism in the Arabian Shield. *Geochemistry Geophysics Geosystems*, 8, Q06021. doi: [10.1029/2006GC001566](https://doi.org/10.1029/2006GC001566).
- Parker RL. 1972. The rapid calculation of potential anomalies. *Geophysical Journal of the Royal Astronomical Society*, 31, 447–455.
- Pal SK, Majumdar TJ, Pathak VK, Narayan S, Kumar U, Goswami OP. 2015. Utilization of high-resolution EGM2008 gravity data for geological exploration over the Singhbhum-Orissa Craton, India. *Geocarto International*, 31(7), 783–802. doi: [10.1080/10106049.2015.1076064](https://doi.org/10.1080/10106049.2015.1076064).
- Pavlis NK, Holmes SA, Kenyon SC, Factor JK. 2008. An Earth Gravitational Model to degree 2160: EGM2008. *Geophysical Research Abstracts*, 10, EGU2008–A-01891.
- Robertson PLC Group. 1990. Geological map of Yemen.
- Sanfilippo A, Sani C, Rasul NMA, Stewart ICF, Vigliotti L, Widinly N, Osemi A and Ligi M. 2021. Hidden but Ubiquitous: The Pre-Rift Continental Mantle in the Red Sea Region, *Frontiers in Earth Science*, 9, 699460. doi: [10.3389/feart.2021.699460](https://doi.org/10.3389/feart.2021.699460).
- Sembroni A, Faccenna C, Becker TW, Molin P, Abebe B. 2016. Long term, deep-mantle support of the Ethiopia-Yemen Plateau. *Tectonics*, 35, 469–488. doi: [10.1002/2015TC004000](https://doi.org/10.1002/2015TC004000).
- Shin YH, Xu H, Braitenberg C, Fang J, Wang Y. 2007. Moho undulations beneath Tibet from GRACE-integrated gravity data. *Geophysical Journal International*, 170(3), 971–985. doi: [10.1111/j.1365-246X.2007.03457.x](https://doi.org/10.1111/j.1365-246X.2007.03457.x).
- Steffen R, Steffen H, Jentzsch G. 2011. A three-dimensional Moho depth model for the Tien Shan from EGM2008 gravity data. *Tectonics*, 30, TC5019. doi: [10.1029/2011TC002886](https://doi.org/10.1029/2011TC002886).
- Stern RJ and Johnson PR. 2019. Constraining the Opening of the Red Sea: Evidence from the Neoproterozoic Margins and Cenozoic Magmatism for a Volcanic Rifted Margin, In Rasul NMA and Stewart ICF (Eds), *Geological Setting, Palaeoenvironment and Archaeology of the Red Sea*. Switzerland, Springer Nature, 53–79.
- Stewart SA. 2016. Structural geology of the Rub' Al-Khali Basin, Saudi Arabia. *Tectonics*, 35, 2417–2438. doi: [10.1002/2016TC004212](https://doi.org/10.1002/2016TC004212).
- Stolk W, Kaban M, Beekman F, Tesauro M, Mooney WD, Cloetingh S. 2013. High resolution regional crustal models from irregularly distributed data: Application to Asia and adjacent areas. *Tectonophysics*, 602(6), 55–68. doi: [10.1016/j.tecto.2013.01.022](https://doi.org/10.1016/j.tecto.2013.01.022).
- Tenzer R, Novak P, Gladkikh V, Vajda P. 2012. Global crust-mantle density contrast estimated from EGM2008, DTM2008, CRUST2. 0, and ICE-5G. *Pure and Applied Geophysics*, 169(9), 1663–1678.
- Tirel C, Gueydan F, Tiberi C, Brun JP. 2004. Aegean crustal thickness inferred from gravity inversion. *Geodynamical Applications, Earth and Planetary Science Letters*, 228(3–4), 267–280. doi: [10.1016/j.epsl.2004.10.023](https://doi.org/10.1016/j.epsl.2004.10.023).
- Zumbo V, Féraud G, Bertrand H, Chazot G. 1995. ⁴⁰Ar/³⁹Ar chronology of the Tertiary magmatic activity in Southern Yemen during the early Red Sea- Aden rifting. *Journal of Volcanology and Geothermal Research*, 65, 265–279. doi: [10.1016/0377-0273\(94\)00106-Q](https://doi.org/10.1016/0377-0273(94)00106-Q).